# ARTICLE IN PRESS

Journal of the European Ceramic Society xxx (xxxx) xxx

ELSEVIER

Contents lists available at ScienceDirect

# Journal of the European Ceramic Society

journal homepage: www.elsevier.com/locate/jeurceramsoc



# Original article

# Thermal and structural performance of additively manufactured ceramic porous media burners

Nicholas DiReda<sup>1</sup>, Giancarlo D'Orazio<sup>1</sup>, Sadaf Sobhani \*

Department of Mechanical and Aerospace Engineering, Cornell University, Ithaca, NY 14850, United States of America

#### ARTICLE INFO

#### Keywords:

Ceramic additive manufacturing Triply periodic minimal surfaces High-temperature systems

#### ABSTRACT

This study examines the effect of porosity, topology and material composition on the performance of additively manufactured ceramic porous media burners. Thermal-structural simulations of triply periodic minimal surfaces (TPMS) were performed to investigate thermal-stress magnitude and distribution. Alumina and mullite TPMS structures were 3D-printed and tested in a methane-air combustion experiment, where the mullite structures showed superior durability compared to alumina. X-ray imaging revealed notable correlation between predicted high tensile stress regions and experimental crack formation. At equivalent porosity and cell size, TPMS structures with higher specific surface area and tortuosity were found to have lower thermal strain and propensity for structural failure. Structures with these features, namely diamond and I-WP, demonstrated favorable thermal and structural behavior under identical thermal conditions. These findings can guide the design and manufacturing of high-temperature applications with embedded porous structures, such as heat exchangers, catalytic converters, and thermal management systems.

#### 1. Introduction

Ceramic materials are widely employed in various engineering applications [1–3] due to their remarkable compressive strength, stiffness, and resilience in corrosive environments. In particular, porous ceramic structures have been applied in high temperatures systems, including heat exchangers, injector face plates, and catalytic converters to modulate thermal transport, reactivity, and stability [4,5]. However, creating complex yet durable ceramic structures that concurrently optimize thermal, fluidic, and structural performance is challenging using conventional methods. Combining the potential for customization from additive manufacturing (AM) with the excellent thermal and corrosion resistance of ceramic materials enables the construction of optimized structures that are robust for application to extreme conditions.

Traditional fabrication techniques of ceramic foams consider bulk properties, such as pore density, and result in random strut orientations and pore distributions, which can significantly alter performance. AM methods, such as digital light processing (DLP), allow for the fabrication of highly engineered structures generated from computer-aided design (CAD) software, circumventing the limitations of traditional methods. Specifically, a series of formula-driven structures known as triply periodic minimal surfaces (TPMS) are often used to generate CAD models. TPMS structures include Schwarz primitive, gyroid, I-graph and Wrapped Package-graph or 'I-WP', diamond, and PMY. Defining

the porous matrix based on one of these TPMS allows significant control over the topology, pore size, wall thickness, and functional gradation. TPMS have been considered in a variety thermofluidic applications [6–8]. However, the complexity of TPMS structures prohibits manufacturing via conventional means beyond a small number of unit cells, thus necessitating the use of AM.

Recently, multiple studies have examined the mechanical and thermal properties of additively manufactured TPMS structures [9–12]. Compression testing of TPMS across a range of porosities demonstrate Diamond and I-WP as two of the strongest sheet-TPMS, whereas primitive is commonly found to be among the weakest [10,11]. Additionally, a similar trend was found for polymeric TPMS structures, where Gyroid has been reported to possess promising mechanical properties as well [13,14]. Numerical simulations of residual thermal stresses induced during fabrication via AM reported the effective mechanical properties of various TPMS geometries and noted reductions in properties such as stiffness. [15]. Interpenetrating phase composites reinforced with thickened sheet-TPMS architectures were found to produce a lower effective coefficient of thermal expansion (CTE) compared to conventional composites leading to higher robustness [16]. Although previous studies have demonstrated the differences in compressive strength among TPMS structures as well as the effects of thermal stresses, the relationship between ceramic TPMS topology and

https://doi.org/10.1016/j.jeurceramsoc.2023.11.001

Received 3 April 2023; Received in revised form 23 October 2023; Accepted 2 November 2023 Available online 10 November 2023 0955-2219/© 2023 Elsevier Ltd. All rights reserved.

<sup>\*</sup> Corresponding author.

E-mail address: sobhani@cornell.edu (S. Sobhani).

<sup>1</sup> Co-first authors.

Table 1
Triply Periodic Minimal Surfaces (TPMS) studied and corresponding implicit functions used to defined the structure.

TPMS	Implicit function			
SP	$\psi_{SP}(x,y,z) = \cos(x) + \cos(y) + \cos(z)$			
G	$\psi_{G}(x,y,z) = \sin(x)\cos(y) + \sin(y)\cos(z) + \sin(z)\cos(x)$			
I	$\psi_1(x,y,z) = 2(\cos(x)\cos(y) + \cos(z)\cos(x) + \cos(y)\cos(z)) - (\cos(2x) + \cos(2y) + \cos(2z))$			
D	$\psi_{\rm D}(x,y,z) = \cos(x)\cos(y)\cos(z) - \sin(x)\sin(y)\sin(z)$			
P	$\psi_{\rm p}({\rm x,y,z}) = 2\cos({\rm x})\cos({\rm y})\cos({\rm z}) + \sin(2{\rm x})\sin({\rm y}) + \sin({\rm x})\sin(2{\rm z}) + \sin(2{\rm y})\sin({\rm z})$			

thermal-structural performance in high temperature systems has not been investigated.

One application of interest for complex ceramic porous structures is porous media burners (PMBs). Prior studies have shown that combustion in porous media offers significant advantages over traditional free-flame combustion in regards to emissions, flame stability, and fuel efficiency [17-20]. PMBs are comprised of an inert porous infill inside solid burner walls, and are characterized by a large internal surface area which promotes conductive and radiative heat transfer throughout the burner. Heat recirculation to the reactants upstream results in excess enthalpy burning and enables stable ultra-lean combustion [21-24], leading to improved fuel efficiency and decreased emissions of NO<sub>x</sub> and CO byproducts [20]. However, studies have shown significant crack formation and material degradation after PMB operation due to the hightemperature flame embedded in the porous structure [4,23,24]. The long-term performance and reliability of PMBs and other thermofluidic systems involving porous structures depend on their structural integrity. Therefore, characterizing the thermal-structural durability of additively manufactured porous ceramic structures is highly relevant to addressing the growing interest in such advanced clean combustion technologies as well as other high temperature energy conversion and thermal management systems.

Here, coupled thermal-structural simulations and experiments of five different cylindrical ceramic TPMS structures were performed to investigate their performance and durability at high temperatures. Variations in tensile stress levels formed under thermal expansion were explored computationally. Temperature measurements from experiments were used to define the thermal conditions applied in computational analysis. For experimentation, structures were fabricated using DLP 3D printing in mullite and alumina, two ceramic materials that exhibit different CTE, which is known to contribute to thermal shock resistance [25]. Flexural bending tests and thermomechanical analysis (TMA) were performed on samples of both materials at elevated temperatures to compare strength degradation, anisotropy and CTE. Furthermore, crack formation in burners post-combustion were examined using X-ray Computed Tomography and compared with high tensile regions predicted by simulations. The methods used for finite element (FE) simulations, designing and manufacturing of the porous structures, and combustion experimental setup are outlined in Section 2, followed by the computational and experimental results in Section 3. Finally, the conclusions and comments about future work are presented in Section 4.

# 2. Methods

## 2.1. TPMS structures

Five TPMS structures were investigated, namely Schwarz primitive (SP), gyroid (G), I-WP (I), diamond (D), and PMY (P). The TPMS implicit functions used for each structure are shown in Table 1.

In this work, sheet-TPMS structures were selected based on their favorable mechanical properties as compared to skeletal-TPMS [26,27].

**Table 2** Specific surface area (SSA), pore diameter ( $D_{pore}$ ), minimum sheet thickness ( $t_{sheet}$ ), and tortuosity for 1 mm 75% porosity unit cells of each TPMS structure.

TPMS	SSA (mm <sup>-1</sup> )	D <sub>pore</sub> (mm)	t <sub>sheet</sub> (mm)	Tortuosity
SP	22.5	0.1	0.35	1.05
G	27.2	0.08	0.26	1.20
I	32.2	0.06	0.28	1.17
D	36.2	0.06	0.29	1.23
P	39.0	0.02	0.08	1.17

Previous work with alumina 3D printed TPMS structures demonstrated both higher strength and stiffness for the case of sheet-gyroids as compared to skeletal-gyroids [28]. Additionally, sheet-TPMS offer a higher specific surface area (SSA), which is advantageous in thermal applications where interphase heat exchange is critical. In the sheet-TPMS framework, a thickness is applied to the minimal surface to achieve a target cell size and relative density [29]. Porous structures studied were designed using MSLattice software [29].

Fig. 1 illustrates the unit cells of the five TPMS structures employed in this study and workflows for simulations and experiments. For 1 mm cell size and 75% porosity structures, the geometric properties of the TPMS structures investigated are summarized in Table 2. The SSA, pore diameter, and minimum sheet thickness were measured within nTopology. Hydraulic tortuosity is defined as the total length of a line divided by the euclidean distance from start to finish; this was estimated using ANSYS Fluent by imposing laminar viscous flow through each unit cell at a Reynolds number < 1. The total length of each streamline was divided by the corresponding euclidean distance, then averaged over the volume to give a characteristic tortuosity [30]. Fig. 1(a) shows the streamlines through each structure, which illustrates tortuosity. The geometric properties of each TPMS structure are later used to analyze combustion and thermal-structural behavior from corresponding computational and experimental results.

# 2.2. Computational modeling

Thermal-structural FE simulations were performed to evaluate the impact of internal topology on thermal-stress formation and dissemination. Additionally, a comparison between pure alumina  $(\mathrm{Al}_2\mathrm{O}_3)$  and mullite  $(11\mathrm{Al}_2\mathrm{O}_3:15\mathrm{iO}_2)$  was made to explore the differences between two commonly used AM ceramic materials that exhibit varying thermal properties. Uniform and graded structures were studied to investigate fundamental understanding of thermal-structural behavior as a function of topological features as well as to facilitate comparisons with the graded experimental burners. The length and diameter of the computational porous structures were 10 mm with a surrounding shell of 0.5 mm thickness.

First, computational designs were imported from MSLattice to software nTopology [31] for meshing. Then, all meshes were constructed with quadratic tetrahedral elements to adequately capture deformation at edge midpoints. A mesh resolution study was conducted to establish convergence of results and an element edge length/pore diameter ratio of approximately 0.05 was found to be satisfactory. Fig. 1(b) illustrates the resolution of an example solid mesh. Meshes were then imported into ANSYS Mechanical where steady-state thermal analysis was coupled with static-structural analysis. A radial constraint boundary condition was imposed on the outer surface of the cylinder, which represents experimentation conditions (see Section 2.4) and other relevant practical applications. Experimental thermocouple measurements from combustion testing were used for the temperature boundary conditions at the top and bottom faces to facilitate comparisons between the simulations and experiments. Averaged measurements from thermocouples 2 and 3, which were closest to the flame, were imposed for the top and bottom boundary conditions, respectively (see Fig. 2(b) for thermocouple locations). Given a positive CTE, this temperature condition induces thermal expansion and elastic strain since free motion is

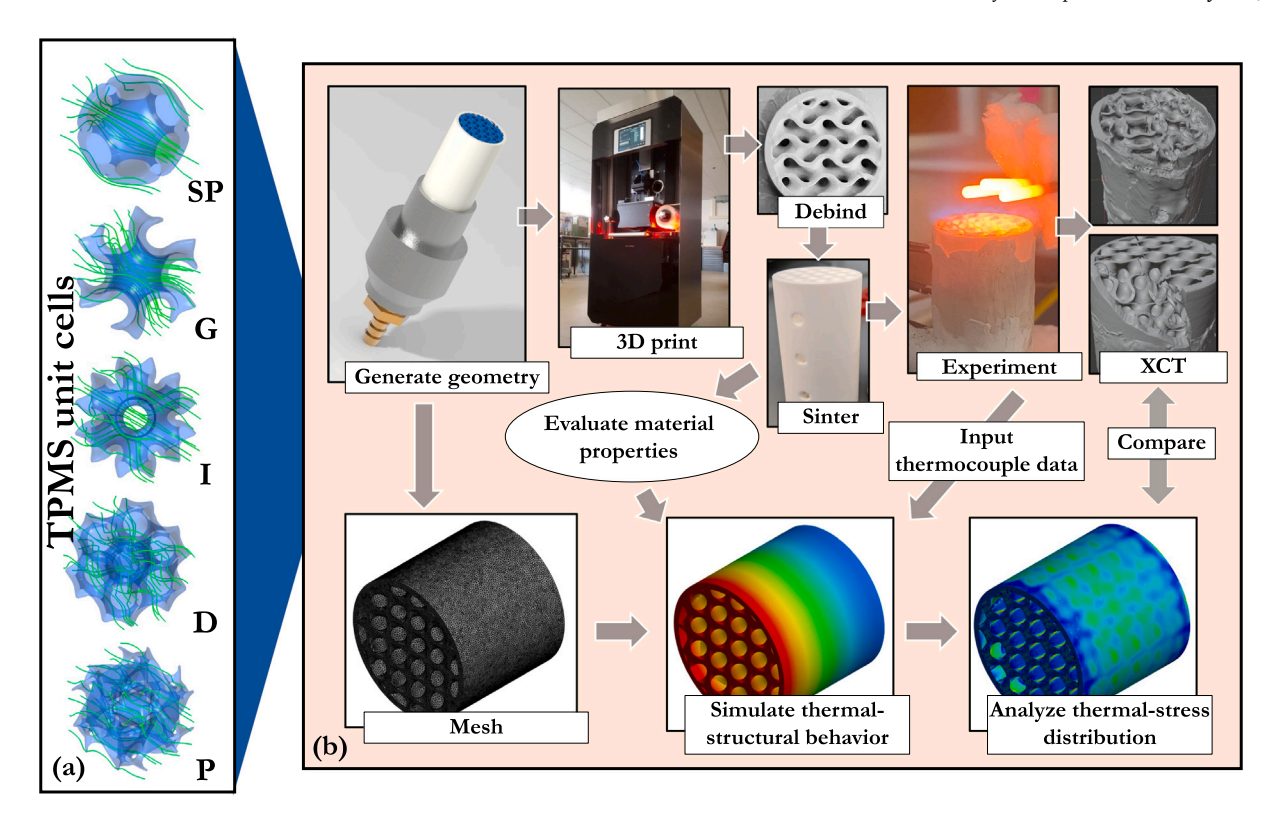


Fig. 1. (a) Computational results illustrating streamlines used to compute tortuosity of 1 mm unit cells of the five TPMS structures investigated. (b) Workflow for the geometry generation, experimentation and computations.

restricted by structural boundary conditions. Stress and strain develop according to the following relations for isotropic materials [32]:

$$\epsilon_{ij}^{thermal} = \alpha (T - T_{ref}) \delta_{ij} \tag{1}$$

$$\epsilon_{ij}^{elastic} = 1/E(\sigma_{ij} - \nu(\sigma_{kk}\delta_{ij} - \sigma_{ij})) \tag{2}$$

$$\epsilon_{ij}^{total} = \epsilon_{ij}^{thermal} + \epsilon_{ij}^{elastic} \tag{3}$$

$$\sigma_{ij} = 2\mu \epsilon_{ij}^{total} + (\lambda e - \beta (T - T_{ref})) \delta_{ij} \quad (i,j=1,2,3) \eqno(4)$$

Where  $\alpha$  is the temperature dependent CTE,  $\nu$  is the Poisson ratio, E is the Young's Modulus for the material,  $\lambda$  and  $\mu$  are the Lamé elastic constants,  $\beta$  is the thermoelastic constant, e is the dilatation; T is the temperature at evaluation, and  $T_{ref}$  is a reference temperature used to define zero-strain. The constants  $\lambda$ ,  $\mu$ , and  $\beta$  are compact terms that are functions of  $\alpha$ ,  $\nu$ , and E. For the simulations, a Young's modulus of 400 GPa at 25 °C and 360 GPa at 500 °C was applied for alumina and 220 GPa and 190 GPa for mullite, respectively [33,34]. These values were also verified using deflection data from bending tests, as discussed in Section 2.4. Values for  $\nu$  were taken to be fixed at 0.23 and 0.25 for alumina and mullite, respectively. As shown in Eqs. (1)–(4), the magnitude of thermal strain is directly related to the material's CTE, so accurate property data as temperature increases is paramount. Therefore experiments on printed samples were performed to determine the CTE as a function of temperature.

## 2.3. Additive manufacturing

High-quality stereolithography files were generated of the burners and scaled by a factor of 1.3 to account for shrinkage during sintering. Structures were printed using an Admaflex 130 DLP printer at a layer height of 30  $\mu$  m and 50  $\mu$  m feature size. The printed structures were first debound in a deionized water bath for 24 h at 40 °C to

remove a portion of the water-soluble resin, subsequently dried for 24–48 h, and then thermally debound in a muffle furnace over a 48 h period. This debinding process removes resin from the printing process in preparation for sintering at a final temperature of 1625 °C. The general design process is illustrated in Fig. 1(b). Previous additively manufactured porous structures used in PMBs [24] were fabricated using only alumina, which resulted in significant degradation of the structures due to thermal cycling. In order to address this durability concern, silica was added to the alumina slurry to create a mixture of mullite (95% alumina, 5% silica). The addition of silica lowers the mixture CTE, thus it is expected to exhibit improved resistance to thermal shock while maintaining superior processing characteristics to the alumina slurry. Additionally, one alumina diamond structure was printed for comparison of material durability.

# 2.4. Characterization and testing

Flexural bending tests were conducted to compare the strength reductions of thermally shocked and un-shocked samples of 3D printed mullite and alumina. Criteria followed ASTM C1525-18 and C1161-18, utilizing a four-point bending test with a loading span half that of the support span [35,36]. Maximum flexural stress was calculated using the formula:

$$\sigma_f = \frac{3FL}{4bd^2} \tag{5}$$

where the flexural stress is given as a function of the load in N (F), length of the support span (L), width of the test beam (b) and depth of the beam (d). In these tests, a support span of 40 mm was utilized with a beam length of 45 mm, and width and depth of 4 and 3 mm respectively. Three samples were printed and tested for each reported condition.

Thermomechanical analysis was conducted via a TA Instruments Q400EM wherein 5 mm sections of alumina and mullite flexural bending beams were heated from 100 to 1000  $^{\circ}$ C with a holding force of 1

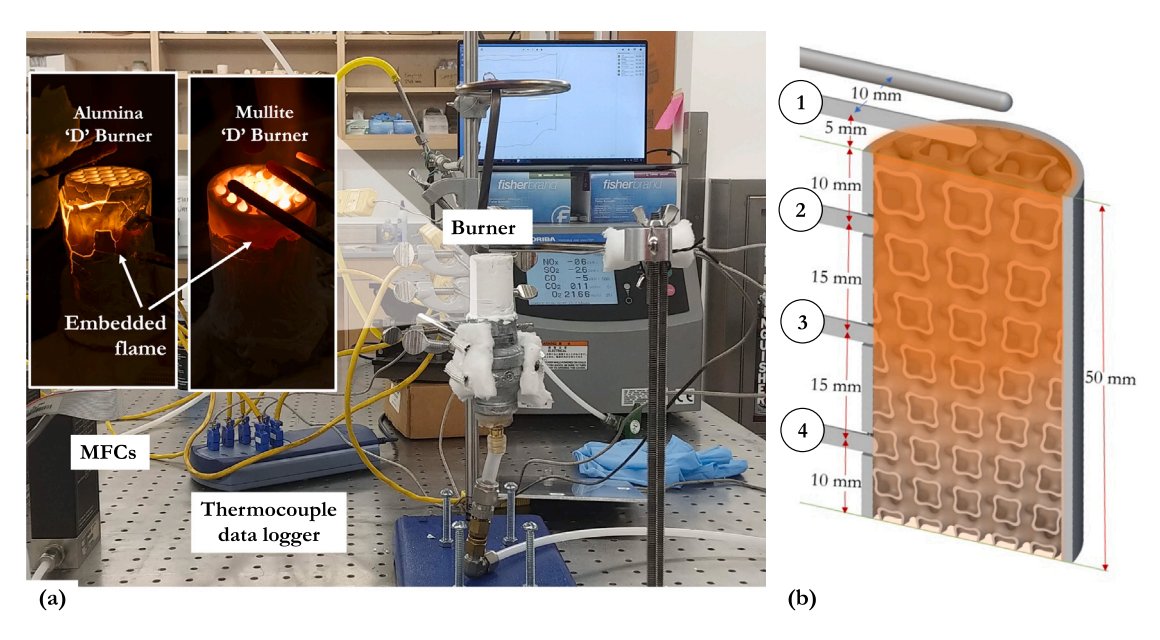


Fig. 2. (a) PMB experimental setup with an embedded flame in the alumina and mullite burners shown during operation. (b) Schematic illustrating thermocouple arrangement.

N for the duration of the experiment. The CTE was calculated based on the linear coefficient of thermal expansion:

$$\alpha = \frac{1}{L} \frac{dL}{dT} \tag{6}$$

where  $\alpha$  is the CTE, dependent on the reciprocal of the original sample length, L, and the change in length, dL, with respect to change in temperature, dT.

Experimental PMBs were designed as a cylinder with an outer shell thickness of 1.5 mm, an outer diameter of 28 mm, and axial height of 50 mm. In each case, the TPMS structure was linearly graded axially, from a cell size of 5 mm at the entrance to 10 mm at the exit, at a constant 75% porosity. Prior research has shown similar grading to support stable combustion over a wide range of operating conditions [24,37,38]. The structures were created in MSLattice and subsequently merged with a tubular structure generated in nTopology.

Fig. 2(a) and (b) illustrate the experimental setup and thermocouple spacing in the burners. Three type K thermocouples (labeled as 1) were positioned at a height of 5 mm above the burner exit and spaced evenly across the diameter, with the left and right thermocouples placed 2.5 mm inward from the edge. Three additional type-K thermocouples (labeled 2-4) were inserted into the sampling ports in the tube, one 10 mm upstream from the burner exit, one at the middle point of the burner, and one 10 mm from the entrance to the burner. All temperature data was captured with a Pico Technology TC-08 thermocouple data logger. A mixture of methane gas and air was introduced to the PMBs via two MKS mass flow controllers (MFCs) at a constant rate during the duration of the experiment. In these experiments, flow rate and fuel-air equivalence ratios were kept constant to isolate the effects of heat flux on porous microstructure. The fuel-air equivalence ratio,  $\phi$ , is defined as the ratio of mass flux of fuel to that of air divided by the stoichiometric ratio of the fuel to air. Here, a fuel-lean value of  $\phi = 0.95$  was targeted by setting a flow rate of 1400 standard cubic centimeters per minute (SCCM) of air and 140 SCCM of methane. PMBs were preheated with a heat gun to reach an internal temperature of at least 100 °C at all thermocouples in order to reduce the potential for thermal shock upon ignition. After ignition, the flame stabilized at the surface of the PMB for up to 10 min. Next, a secondary external heat source was applied to move the flame into the porous media. In most cases, this heat source was used until the temperature of the top thermocouple was 300-400 °C. At this point, the flame moved upstream, embedding in the porous structure. The system was then

allowed to reach an equilibrium stabilization temperature defined to be the point at which the temperature at the top burner thermocouple port did not fluctuate more than 5  $^{\circ}$ C over a 15 min period.

X-ray computed tomography (XCT) imaging of burners after experiments was conducted to determine the extent of material failure for each burner. Imaging was performed using a Zeiss Versa 520, scanning at 120 kV with an exposure time of 1.2 s, with a resulting 30-35  $\mu m$  per pixel resolution. The digital imaging files generated from the XCT scans were segmented in 3D Slicer [39,40] to produce high contrast images that highlight any cracks developed within the fired burners.

# 3. Results and discussion

# 3.1. Flexural bending and TMA tests

Fig. 3 illustrates the results from flexural bending and TMA tests of 3D printed mullite and alumina bars printed perpendicular ('Z') and parallel ('XY') to the printing plane. The results show that while mullite has lower flexural strength than pure alumina, its strength degradation due to thermal shock is less pronounced than that of alumina, as shown in Fig. 3(a). When heated to 700 °C, strength in the XY plane exhibited a ~ 90% strength reduction for alumina and ~77% for mullite as compared to room temperature strength. This demonstrates that pure alumina suffers from greater material degradation at elevated temperatures. Bars printed in the 'Z' orientation had approximately 74% lower strength than those in 'XY', thus illustrating significant anisotropy in the strength of ceramic AM materials. Average strength values in the XY plane at ambient conditions were used to evaluate the FI in the simulation analysis. Fig. 3(b) illustrate the higher CTE of alumina compared to mullite over the operating regime of the porous media burners. The logarithmic curve fits for each experimental run were used as inputs for the ANSYS thermal models to better characterize the thermomechanical behavior of 3D printed ceramics.

#### 3.2. Thermal-structural simulations

The computational results are presented using the failure index FI, which is used to quantify regions of material failure based on maximum principal stresses,  $\sigma_{MPS}$ , adapted from [41].

The material is likely to fail when FI is equal to or greater than 1, defined as:

$$FI = \frac{\sigma_{MPS}}{\sigma_{MAN}} \tag{7}$$

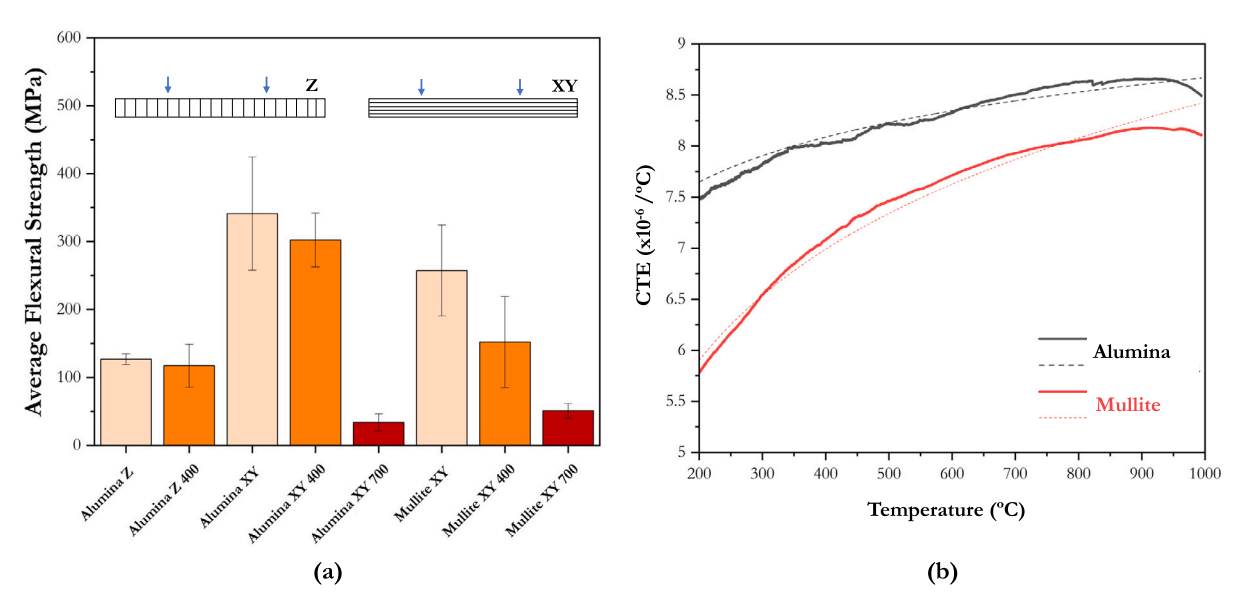


Fig. 3. (a) Average flexural bending strength of alumina and mullite, comparing 'Z' and 'XY' print orientation, and effects of thermal shock at 400 °C and 700 °C. (b) Experimental TMA data for alumina and mullite (solid lines) with logarithmic curve fits for each (dashed lines).

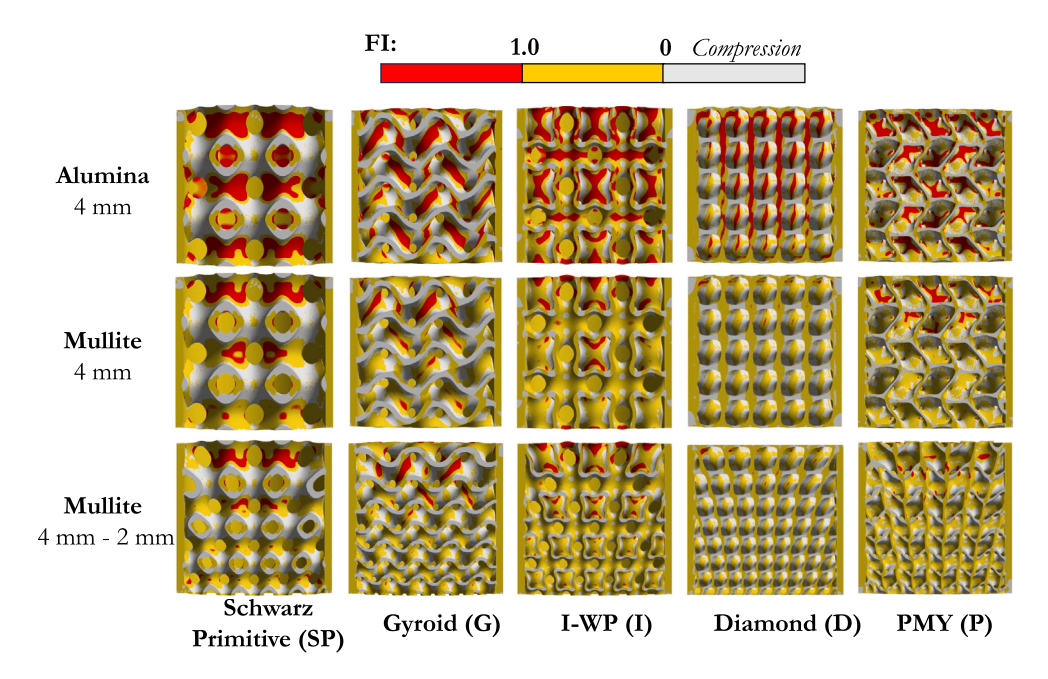


Fig. 4. Failure Index FI based on maximum principal stresses of uniform cell size structures (4 mm cell size) and graded mullite structures (4 mm-2 mm).

where  $\sigma_{\rm MAX}$  is the maximum average strength of the material as determined by flexural bending tests. Since the ultimate compressive strength of ceramics is typically an order of magnitude higher than the ultimate tensile strength, the structure promoting the highest states of tensile stress is assumed have the highest propensity for crack formation. These states of tensile stress are captured by  $\sigma_{\rm MPS}$  developed within each element. FI is calculated at each element for the simulated uniform and graded TPMS structures, and results are shown in Figs. 4–8. Regions shown in grey exhibit only principal stresses in compression, where all others experience varying degrees of tensile stress.

Fig. 4 correspond to structures with 75% porosity and either a linear gradation in cell size from 4 mm to 2 mm or a uniform cell size of 4 mm. For all structures tested, the highest stresses are seen near the center of the structure, which suggests that peak stress levels are most sensitive to the underlying TPMS topology as opposed to the junction at the cylindrical wall. Significantly more regions of failure (i.e. FI > 1)

are predicted for structures made of alumina as compared to mullite. Among the mullite structures, 'D' and 'P' have smaller regions of failure.

Results shown in Fig. 4 are further quantified by binning the nodes in different FI categories. Since element edge lengths for each mesh were nearly identical with less than 15% deviation from the mean for one standard deviation, the number of nodes in each FI range are normalized by the total nodes to approximate the percentage of elements under compression or at various degrees of tension approaching failure. These results are shown in Fig. 5 for uniform and graded structures, respectively. Results for uniform and graded structures were consistent for each TPMS topology. This analysis confirms that more elements in the alumina structures were found to have FI > 1 as compared to mullite. This supports our experimental finding and can be attributed to the lower CTE of mullite, as seen in Fig. 3(b) which produces lower thermal expansion given identical temperature conditions. The volume with FI > 0.8 for SP structures was considerably higher for both graded

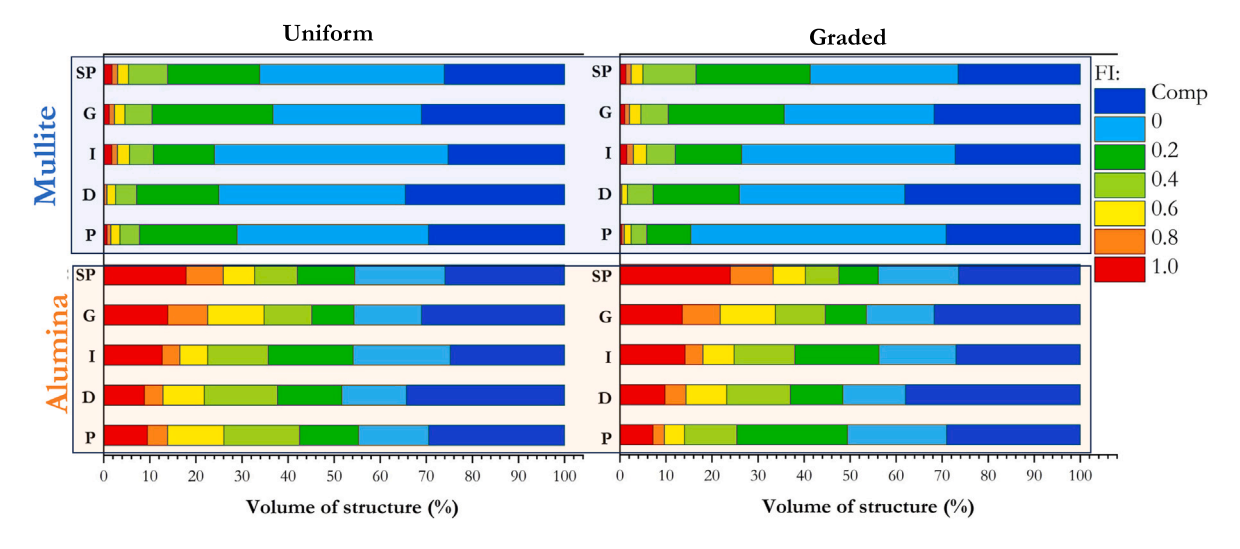


Fig. 5. Volume percentage of failure indices for uniform and graded cell size alumina and mullite structures.

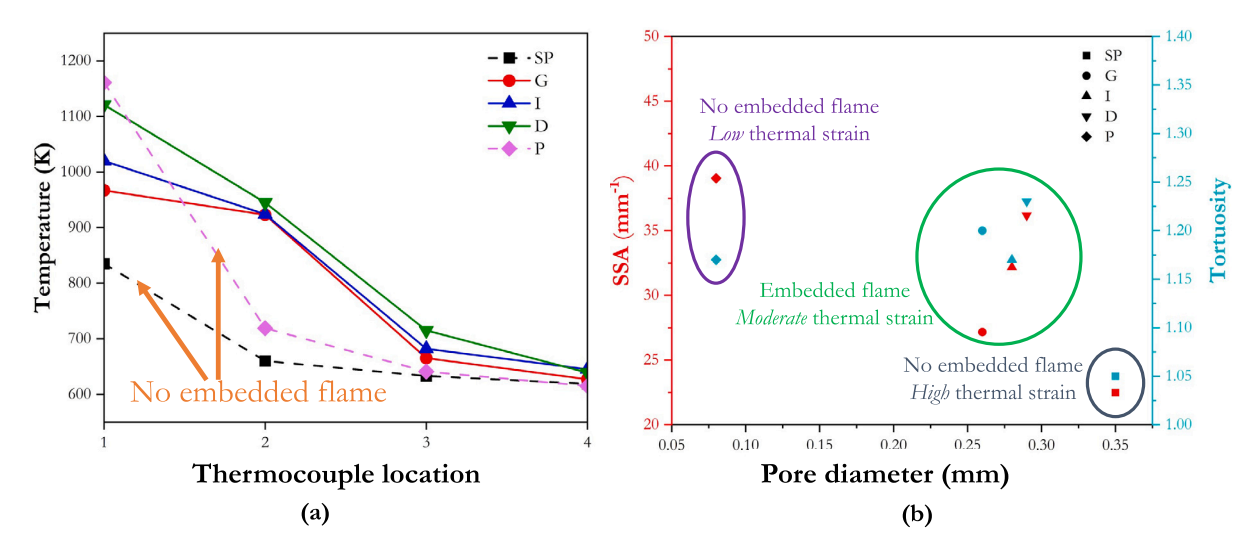


Fig. 6. (a) Thermocouple temperature measurements at steady-state burner operation, dotted lines indicate unsuccessful non-embedded flames. (b) Specific surface area (SSA), pore diameter, and tortuosity of each 1 mm 0.75 porosity unit cell, with regions of flame stability indicated.

and ungraded conditions. This indication of lower strength is consistent with previous work examining the compression testing of TPMS which concluded sheet-based SP samples had lower ultimate strength than I and G structures [11]. SP stress distributions indicate failure propensity due to a poor ability to mitigate thermal strain in forms other than tensile stress.

Unrestricted and frictionless motion in the Z axis allows axial deformation which can be used as a proxy for the stiffness of each structure. The geometric characteristics from Table 2 are shown graphically in Fig. 6(b) to highlight regions of low, moderate and high thermal strain. Fig. 7(a) illustrates axial thermal strain calculated as the axial deformation normalized by the original length for 75% structures. High SSA, low pore diameter, high tortuosity generally correspond to low thermal strain and stress distribution. Here, the SP and P structures were found to be the least and most stiff, respectively. SP has low SSA, large pore diameter, and low tortuosity providing the freedom for expansion under thermal loads. Greater deformation is shown to scale with stress severity for each structure. The stiffer structures such as P have higher SSA, smaller pores, and greater tortuosity, and thus lower stress and FI fields.

Simulations were also performed to understand the effects of porosity and cell size changes on thermal-structural behavior. These simulations were conducted from ambient to a uniform condition of 550

°C. Results shown in Fig. 7(b) represent uniform structures at three different porosities (68%, 75%, 82%) and 4 mm cell size. Cell size gradation and porosity within a given TPMS structure are found to have a weaker influence on stress development than internal topology and material properties. Results demonstrate that axial thermal strain increases with porosity for all structures due to larger void space and thinner struts. However, the trend in thermal strain between the structures is mostly independent of porosity, with the exception of D and P structures at the lowest porosity.

Results in Fig. 8 correspond to uniform structures at 75% porosity and three different cell sizes 4 mm, 3 mm, 2 mm. At smaller cell sizes within a fixed dimension structure, the increased number of connections between adjacent cells improves lateral support and stiffness. Thus, there is a decrease in thermal strain with decreasing cell size. As with porosity, the trend in thermal strain between the structures is mostly independent of cell size (i.e. SP consistently the largest).

## 3.3. Combustion experiments

To thermally stress each burner, we exploited the high temperatures from combustion in the PMB configuration as described in Section 2.4. The experiments illustrated significant performance variations for burners of different internal topology under constant operating

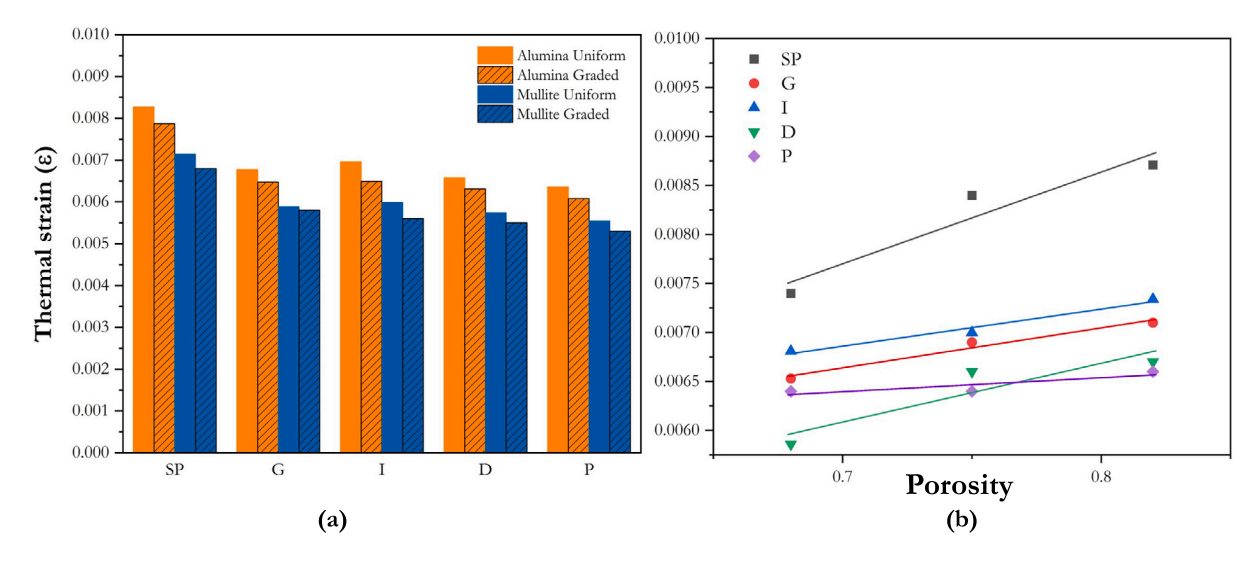


Fig. 7. (a) Axial thermal strain for uniform and graded structures in alumina and mullite at 75% porosity. (b) Thermal strain at 4 mm cell size and variable porosity.

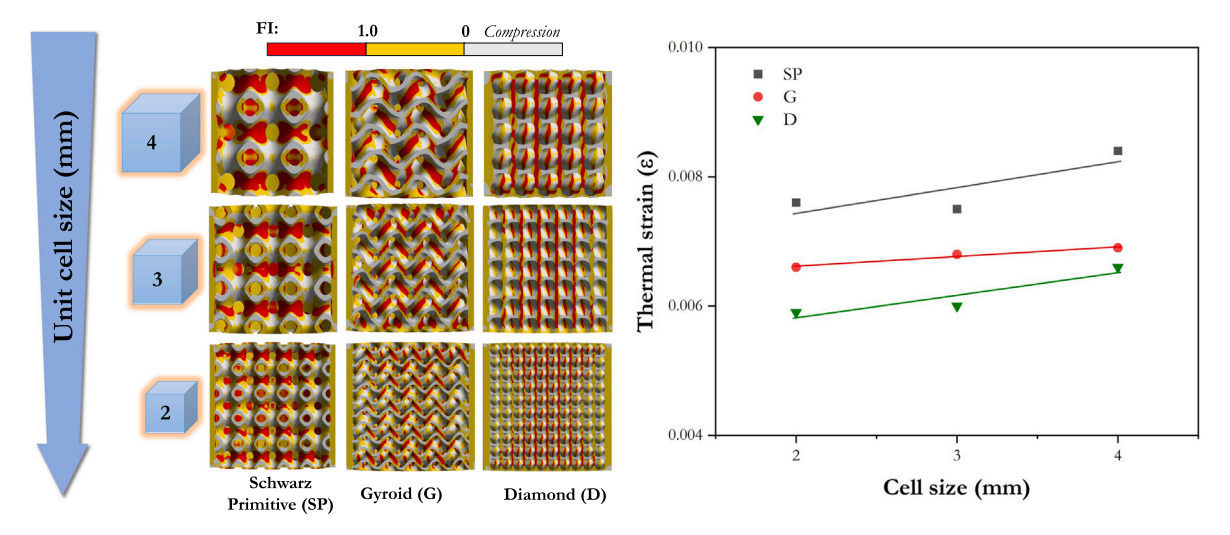


Fig. 8. Failure Index (FI) based on maximum principal stresses of structures with 75% porosity and different cell size, and corresponding thermal strain calculated at uniform temperature conditions.

conditions. Fig. 6(a) displays the average stabilization temperature measurements from all internal thermocouples over the duration of operation, which was approximately 15 min for each burner that sustained an embedded flame. These measurements did not fluctuate more than 5 °C over this time interval. Since the burners were not insulated, radiative heat losses result in lower temperatures than reported in comparable works with TPMS-based porous media burners [4,38]. The heat from combustion recirculated upstream in all cases, as evidenced by preheated reactant temperatures. For the burners that sustained an embedded flame, the temperature profiles differed by approximately 10% within the solid, but followed similar trends in regards to the gradient between thermocouples 2 and 4.

Of the five tested structures, only three were successful in maintaining an embedded flame, or combustion within the porous media, namely D, G, and I. In contrast, SP and P burners did not achieve embedded flames. As illustrated in Fig. 6(b), the geometric properties of the SP and P structures are hypothesized to prohibit embedded flames. Among the TPMS structures tested, SP has the minimum SSA and tortuosity, which lead to shorter fuel residence time within the burner and lower the interphase heat exchange. These characteristics limit the heat release and recirculation needed in porous burners to sustain an embedded flame. Conversely, as the structure with the maximum SSA

and tortuosity, the P structure enables excessive heat transfer from the gas to the solid phase, thus acting as a flame arrestor.

# 3.4. Durability and X-ray image analysis

All burners exhibited noticeable wear in the regions experiencing the highest heat flux with differing levels of crack severity. The D and I burners were found more durable than the G. Furthermore, the mullite D burner was significantly more durable than the alumina D burner. Considerable fracture exhibited by the G burner precluded imaging by XCT, and the P and SP burners were disregarded since embedded flames could not be sustained. Fig. 9 illustrates the cracking seen in the D and I burners after approximately one hour of steady operation. Minor cracks are highlighted in red to improve visibility. Multiple cracks can be seen to cross the D structure struts in the layer plane, which is reported to be of lower strength compared to the layer-orthogonal direction when considering results from the four point flexural bending tests, see Fig. 3. Altering the print orientation of future models may provide greater resilience if weak points are identified and structures are printed so that they exhibit favorable mechanical properties in such loading direction.

The X-ray images show cracks in both longitudinal and transverse planes for D and I mullite burners. Fig. 9(b) and (c) show a comparison

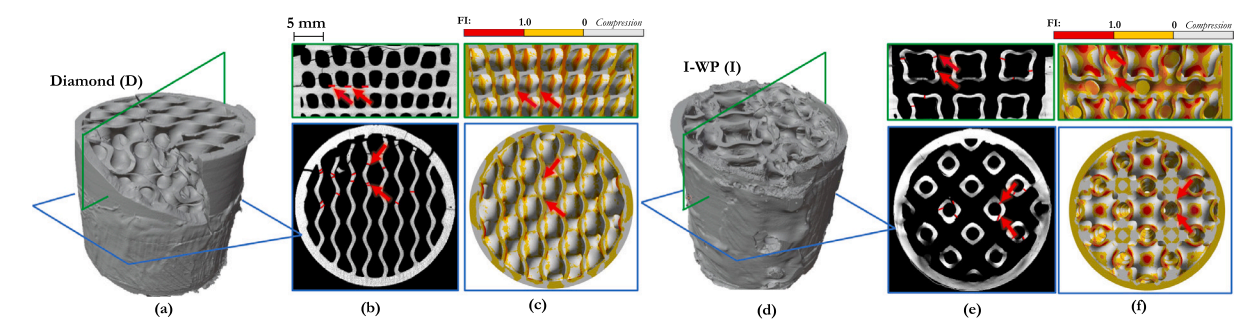


Fig. 9. (a) XCT isosurface of mullite 'D' burner, with longitudinal and transverse cross sections from (b) XCT and (c) simulations. (d) XCT isosurface of mullite 'I' burner, with longitudinal and transverse cross sections from (e) XCT and (f) simulations. Minor cracks in the are highlighted in red for clarity.

between the X-ray images and the FE simulation for longitudinal and transverse cross-sections of the D burner. Analogously, Fig. 9(e) and (f) show these results for the I burner. For both structures, there is noticeable overlap between regions of predicted high FI and the crack locations in the X-ray images, denoted by the red arrows. It is likely that initiation occurred at such locations within a unit cell then propagated throughout the structure as operation continued. Unlike ductile materials, ceramics do not undergo plastic deformation, but rather sudden planar fracture perpendicular to tensile loading directions. Minor crack locations and high stress regions are shown to exhibit consistent spacing. Highlights within a unit cell in Fig. 9(e) appeared approximately 90° apart as did high FI regions in Fig. 9(f). These comparisons demonstrate the fidelity of FE simulations in predicting regions of high stress and subsequently burner failure zones.

#### 4. Conclusion

In this study, ceramic additive manufacturing was applied to print five different TPMS porous structures, namely Schwarz primitive (SP), gyroid (G), I-WP (I), diamond (D), and PMY (P). Durability was investigated by assessing the mechanical behavior through FE simulations and combustion experimentation. The main conclusions drawn from this work are summarized as follows:

- Axial thermal strain from simulations was used as a proxy for stiffness and an indicator of potential failure. TPMS structures with high specific surface area, high tortuosity, and low pore diameter were found to have lower thermal strain and thus decreased failure index values.
- The combustion performance of porous burners is found to be sensitive to geometric features of the TPMS structure. SP and P burners did not facilitate an embedded flame at the same operating conditions as the D, I and G burners, which is hypothesized to be a result of the extremes of specific surface area and tortuosity characteristic of these structures.
- The mullite burner at a composition of  $11 Al_2 O_3:15iO_2$  had much higher durability as compared to the pure alumina burner. This finding was supported by simulations using experimentally derived material properties for mullite and alumina.
- Comparisons between simulations and XCT imaging of burners after operation showed strong correlation between the predicted tensile stress concentrations and experimental crack formation. Crack spacing patterns were also identified, which supports the use of FE simulations to predict thermal-structural performance.

These results demonstrate the potential for tailoring complex porous structures via ceramic AM in the application of high temperature systems, both to augment thermofluidic behavior and for system durability. Future work is required to develop alternate ceramic slurries for DLP printing, which have more favorable thermal shock performance as compared to alumina or mullite, to further improve durability.

Beyond porous burners, future work also includes the application of this methodology to developing optimized ceramic heat exchangers, heat pipes, and other complex ceramic structures in energy and thermal management systems.

# CRediT authorship contribution statement

**Nicholas DiReda:** Investigation, Software, Formal analysis, Conceptualization, Visualization, Writing – original draft. **Giancarlo D'Orazio:** Investigation, Writing – original draft. **Sadaf Sobhani:** Conceptualization, Supervision, Writing – review & editing.

## Declaration of competing interest

The authors declare that they have no known competing financial interests or personal relationships that could have appeared to influence the work reported in this paper.

# Acknowledgments

Imaging data was acquired through the Cornell Institute of Biotechnology's Imaging Facility, with NIH 1S10OD012287 funding for the Zeiss-Xradia Versa 520 X-ray microscope. This work made use of the Cornell Center for Materials Research Facilities supported by the National Science Foundation, United States under Award Number DMR-1719875.

# References

- R. Savino, L. Criscuolo, G.D. Di Martino, S. Mungiguerra, Aero-thermo-chemical characterization of ultra-high-temperature ceramics for aerospace applications, J. Eur. Ceramic Soc. 38 (8) (2018) 2937–2953.
- [2] H. Aono, M. Sato, E. Traversa, M. Sakamoto, Y. Sadaoka, Design of ceramic materials for chemical sensors: effect of SmFeO3 processing on surface and electrical properties, J. Am. Ceram. Soc. 84 (2) (2001) 341–347.
- [3] A. Marques, G. Miranda, F. Silva, P. Pinto, Ó. Carvalho, Review on current limits and potentialities of technologies for biomedical ceramic scaffolds production, J. Biomed. Mater. Res. B Appl. Biomater. 109 (3) (2021) 377–393.
- [4] S. Sobhani, S. Allan, P. Muhunthan, E. Boigne, M. Ihme, Additive manufacturing of tailored macroporous ceramic structures for high-temperature applications, Adv. Eng. Mater. 22 (8) (2020) 2000158.
- [5] M. Belmonte, Advanced ceramic materials for high temperature applications, Adv. Eng. Mater. 8 (8) (2006) 693–703.
- [6] I. Kaur, P. Singh, Flow and thermal transport characteristics of Triply-Periodic Minimal Surface (TPMS)-based gyroid and Schwarz-P cellular materials, Numer. Heat Transfer A Appl. 79 (8) (2021) 553–569, Publisher: Taylor & Francis \_eprint: DOI: http://dx.doi.org/10.1080/10407782.2021.1872260.
- [7] M. Alteneiji, M.I.H. Ali, K.A. Khan, R.K.A. Al-Rub, Heat transfer effectiveness characteristics maps for additively manufactured TPMS compact heat exchangers, Energy Storage Saving 1 (3) (2022) 153–161.
- [8] R. Attarzadeh, S.-H. Attarzadeh-Niaki, C. Duwig, Multi-objective optimization of TPMS-based heat exchangers for low-temperature waste heat recovery, Appl. Therm. Eng. 212 (2022) 118448.

## N. DiReda et al.

- [9] L. Zhang, S. Feih, S. Daynes, S. Chang, M.Y. Wang, J. Wei, W.F. Lu, Pseudo-ductile fracture of 3D printed alumina triply periodic minimal surface structures, J. Fur. Ceramic Soc. 40 (2) (2020) 408–416
- [10] M. Shen, W. Qin, B. Xing, W. Zhao, S. Gao, Y. Sun, T. Jiao, Z. Zhao, Mechanical properties of 3D printed ceramic cellular materials with triply periodic minimal surface architectures, J. Eur. Ceramic Soc. 41 (2) (2021) 1481–1489.
- [11] R. Wang, H. Ye, J. Cheng, H. Li, P. Zhu, B. Li, R. Fan, J. Chen, Y. Lu, Q. Ge, Ultrastrong and damage-tolerant ceramic architectures via 3D printing, Addit. Manuf. (2022) 103361.
- [12] J. Lu, P. Dong, Y. Zhao, Y. Zhao, Y. Zeng, 3D printing of TPMS structural ZnO ceramics with good mechanical properties, Ceram. Int. 47 (9) (2021) 12897–12905.
- [13] D.W. Abueidda, M. Elhebeary, C.-S.A. Shiang, S. Pang, R.K. Abu Al-Rub, I.M. Jasiuk, Mechanical properties of 3D printed polymeric Gyroid cellular structures: Experimental and finite element study, Mater. Des. 165 (2019) 107597.
- [14] D.W. Abueidda, M. Bakir, R.K.A. Al-Rub, J.S. Bergström, N.A. Sobh, I. Jasiuk, Mechanical properties of 3D printed polymeric cellular materials with triply periodic minimal surface architectures, Mater. Des. 122 (2017) 255–267.
- [15] N. Ahmed, I. Barsoum, R.K. Abu Al-Rub, Numerical investigation on the effect of residual stresses on the effective mechanical properties of 3D-printed TPMS lattices, Metals 12 (8) (2022) 1344.
- [16] D.W. Abueidda, A.S. Dalaq, R.K. Abu Al-Rub, I. Jasiuk, Micromechanical finite element predictions of a reduced coefficient of thermal expansion for 3D periodic architectured interpenetrating phase composites, Compos. Struct. 133 (2015) 85–97.
- [17] D. Trimis, F. Durst, Combustion in a porous medium-advances and applications, Combust. Sci. Technol. 121 (1–6) (1996) 153–168.
- [18] G. Brenner, K. Pickenäcker, O. Pickenäcker, D. Trimis, K. Wawrzinek, T. Weber, Numerical and experimental investigation of matrix-stabilized methane/air combustion in porous inert media, Combust. Flame 123 (1) (2000) 201–213.
- [19] Y. Kotani, T. Takeno, An experimental study on stability and combustion characteristics of an excess enthalpy flame, Symposium (International) Combust. 19 (1) (1982) 1503–1509.
- [20] D. Mohaddes, C.T. Chang, M. Ihme, Thermodynamic cycle analysis of superadiabatic matrix-stabilized combustion for gas turbine engines, Energy 207 (2020) 118171
- [21] M. Zabetakis, S. Lambiris, G. Scott, Flame temperatures of limit mixtures, in: Symposium (International) on Combustion, Vol. 7, No. 1, Elsevier, 1958, pp. 484–487.
- [22] S. Wood, A.T. Harris, Porous burners for lean-burn applications, Prog. Energy Combust. Sci. 34 (5) (2008) 667–684.
- [23] S. Sobhani, B. Haley, D. Bartz, J. Dunnmon, J. Sullivan, M. Ihme, Investigation of lean combustion stability, pressure drop, and material durability in porous media burners, in: Turbo Expo: Power for Land, Sea, and Air, Vol. 50893, American Society of Mechanical Engineers, 2017, V05CT17A001.

- [24] S. Sobhani, P. Muhunthan, E. Boigné, D. Mohaddes, M. Ihme, Experimental feasibility of tailored porous media burners enabled via additive manufacturing, in: Proceedings of the Combustion Institute, Elsevier, 2020.
- [25] T. Lu, N. Fleck, The thermal shock resistance of solids, Acta Mater. 46 (13) (1998) 4755–4768.
- [26] S.C. Kapfer, S.T. Hyde, K. Mecke, C.H. Arns, G.E. Schröder-Turk, Minimal surface scaffold designs for tissue engineering, Biomaterials 32 (29) (2011) 6875–6882.
- [27] O. Al-Ketan, R. Rowshan, R.K. Abu Al-Rub, Topology-mechanical property relationship of 3D printed strut, skeletal, and sheet based periodic metallic cellular materials, Addit. Manuf. 19 (2018) 167–183.
- [28] O. Al-Ketan, M. Pelanconi, A. Ortona, R.K.A. Al-Rub, Additive manufacturing of architected catalytic ceramic substrates based on triply periodic minimal surfaces, J. Am. Ceram. Soc. 102 (10) (2019) 6176–6193.
- [29] O. Alketan, MSLattice: A free software for generating uniform and graded lattices based on triply periodic minimal surfaces, Mater. Des. Process. Commun. (2020).
- [30] S.S. Rathore, B. Mehta, P. Kumar, M. Asfer, Flow characterization in triply periodic minimal surface (TPMS)-based porous geometries: Part 1—Hydrodynamics, Transp. Porous Media 146 (3) (2023) 669–701.
- [31] nTopology [Computer software], 2022.
- [32] M.R. Eslami, R.B. Hetnarski, J. Ignaczak, N. Noda, N. Sumi, Y. Tanigawa, Theory of Elasticity and Thermal Stresses, Vol. 197, Springer, 2013, 392-393, pp. 392-393.
- [33] W. Pabst, E. Gregorová, M. Černý, Isothermal and adiabatic Young's moduli of alumina and zirconia ceramics at elevated temperatures, J. Eur. Ceramic Soc. 33 (15–16) (2013) 3085–3093.
- [34] M. Osendi, C. Baudin, Mechanical properties of mullite materials, J. Eur. Ceramic Soc. 16 (2) (1996) 217–224.
- [35] Standard Test Method for Flexural Strength of Advanced Ceramics at Ambient Temperature, Vol. 15.01, ASTM International, West Conshohocken, PA, 2019.
- [36] Standard Test Method for Determination of Thermal Shock Resistance for Advanced Ceramics by Water Quenching, Vol. 15.01, ASTM International, West Conshohocken, PA, 2018.
- [37] S. Sobhani, D. Mohaddes, E. Boigne, P. Muhunthan, M. Ihme, Modulation of heat transfer for extended flame stabilization in porous media burners via topology gradation, Proc. Combust. Inst. 37 (4) (2019) 5697–5704.
- [38] S. Sobhani, P. Muhunthan, D. Mohaddes, E. Boigne, Z. Cheng, M. Ihme, Enabling tailored porous media burners via additive manufacturing, in: 11th U.S. National Combustion Meeting, Pasadena, CA, 2019.
- [39] 3D slicer, 2023, https://www.slicer.org/. (Accessed on 20 January 2023).
- [40] A. Fedorov, R. Beichel, J. Kalpathy-Cramer, J. Finet, J.-C. Fillion-Robin, S. Pujol, C. Bauer, D. Jennings, F. Fennessy, M. Sonka, J. Buatti, S. Aylward, J.V. Miller, S. Pieper, R. Kikinis, 3D Slicer as an image computing platform for the quantitative imaging network, Magn. Reson. Imaging 30 (9) (2012) 1323–1341.
- [41] S. Sharma, P. Talukdar, Thermo-mechanical analysis of a porous volumetric solar receiver subjected to concentrated solar radiation, Sol. Energy 247 (2022) 41–54.